Europe PMC Funders Group
Author Manuscript
Nat Mater. Author manuscript; available in PMC 2022 December 06.

Published in final edited form as:
Nat Mater. 2022 July ; 21(7): 826–835. doi:10.1038/s41563-022-01272-8.

Tapered fibertrodes for opto-electrical neural interfacing in small brain volumes with reduced artefacts

Barbara Spagnolo[#1,*], **Antonio Balena**[#1], **Rui T. Peixoto**[#3,4], **Marco Pisanello**[#1], **Leonardo Sileo**[1], **Marco Bianco**[1,2], **Alessandro Rizzo**[1,2], **Filippo Pisano**[1], **Antonio Qualtieri**[1], **Dario Domenico Lofrumento**[5], **Francesco De Nuccio**[5], **John A. Assad**[3], **Bernardo L. Sabatini**[3], **Massimo De Vittorio**[1,2,†,*], **Ferruccio Pisanello**[1,†,*]

[1]Istituto Italiano di Tecnologia, CBN, Arnesano, 73010 Lecce (Italy)

[2]Dipartimento di Ingegneria dell'Innovazione, Università del Salento, Lecce (Italy)

[3]Howard Hughes Medical Institute, Department of Neurobiology, Harvard Medical School, Boston, MA 02115, (USA)

[4]Department of Psychiatry, University of Pittsburgh, 450 Technology Dr, Pittsburgh, PA 15219, (USA)

[5]DiSTeBA - Dept. of Biological and Environmental Sciences and Technologies. Università del Salento, Lecce (Italy)

[#] These authors contributed equally to this work.

Abstract

Deciphering neural patterns underlying brain functions is essential to understand how neurons are organized into networks. This has been greatly facilitated by optogenetics and its combination with optoelectronic devices to control neural activity with millisecond temporal resolution and cell-type specificity. However, targeting small brain volumes causes photoelectric artefacts, in particular when light emission and recording sites are close to each other. We take advantage of the photonic properties of tapered fibers to develop integrated "fibertrodes" able to optically activate small brain volumes with abated photoelectric noise. Electrodes are positioned very close to light-emitting points by non-planar microfabrication, with angled light emission allowing

Users may view, print, copy, and download text and data-mine the content in such documents, for the purposes of academic research, subject always to the full Conditions of use: https://www.springernature.com/gp/open-research/policies/accepted-manuscript-terms.

[*]Corresponding author, barbara.spagnolo@iit.it, ferruccio.pisanello@iit.it, massimo.devittorio@iit.it.
[†]co-last authors

Author Contributions Statement

A.B., B.S., M.P., R.P. equally contributed to this work. A.B., M.P., M.B., A.R., M.D.V., F. Pisano F. Pisanello developed the two-photon polymerization (2PP) system and the related fibertrodes. L.S., B.S., M.P., A.Q., F. Pisano, M.D.V., F. Pisanello developed the Focused Ion Beam (FIB) fabrication protocol and the related fibetrodes. B.S., A.B., M.P, M.B. and F. Pisanello performed the optoelectrical characterization of the probes. B.S. and R.P. performed in vivo experiments. B.S., A.B., M.P., F. Pisano, F. Pisanello, R.P., B.L.S., J.A. and M.D.V. analyzed and discussed the in vivo data. B.L.S., R.P., B.S., D.D.L., F.D.N., F. Pisanello developed the in vivo experiments protocols. A.B., B.S., L.S., F. Pisanello, M.D.V., B.L.S., J.A. wrote the manuscript and prepared the figures with contributions from all authors. M.D.V., B.L.S., J.A, and F. Pisanello conceived the study and jointly supervised the work.

Competing Interests Statement

LS, BLS, MDV, and F. Pisanello are founders and hold private equity in Optogenix, a company that develops, produces and sells technologies to deliver light into the brain. Tapered fibers commercially available from Optogenix were used as tools in the research. The remaining authors declare no competing interests.

Europe PMC Funders Author Manuscripts
Europe PMC Funders Author Manuscripts

simultaneous optogenetic manipulation and electrical readout of one to three neurons, with no photoelectric artefacts *in vivo.* The unconventional implementation of two-photon polymerization on the curved taper edge enables the fabrication of recoding sites all-around the implant, making fibertrodes a promising complement to planar microimplants.

Europe PMC Funders Author Manuscripts

Europe PMC Funders Author Manuscripts

The use of light to control the activity of genetically defined neuronal populations introduced a new standard to study neural networks. The adoption of optogenetics prompted the development of novel optical devices, aimed at controlling the dynamics of light delivery to the brain with reduced implantation damage and improved biocompatibility. Many of these optical probes feature integrated electrodes (optrodes) to stimulate and record neuronal activity simultaneously, enabling closed-loop control and opto-tagging of specific neural populations with millisecond precision [1]–[6].

One of the first implantable optrodes was based on flat-cleaved optical fibers glued on top of linear electrodes arrays [7]–[12]. Although prone to light-induced photoelectric artefacts due to direct illumination of the electrodes, this configuration is commonly used, and recent studies achieved low-noise recordings by *post-hoc* correction of light-induced signals [13], [14]. However, the fiber-electrodes relative position results in an uneven and asymmetric light distribution across the electrode array and illuminates large brain volumes compared to the size and pitch of the electrodes, likely causing wide network activation, beyond the local circuit of interest [12]. Integration of light sources in close proximity or adjacent to recording sites could provide a solution to these limitations.

Several strategies have been proposed to combine extracellular recording electrodes with local illumination. Solid state waveguides [5] and polymeric fiber optics [15] have been used to position light-delivery points near electrode sites that have been processed with indium tin oxide [16], thus removing high-frequency photoelectric artefacts and strongly mitigating low frequency light-induced noise. However, the stimulation volume remains large, comparable to that of standard fiber optics [17], [18]. Ridge waveguides providing close stimulation and readout points with outcoupling gratings have also been employed [19], but post-processing of signal is required to remove artefacts at light onset and offset. Implantable micro light-emitting diodes (μLEDs) probes can also restrict illumination volumes, but the high current required for driving the emitter influences the recorded electrical signal, causing high frequency artefacts up to 50 μV, limiting the range of optical stimulus waveforms that can be applied [20]–[22]. The Lambertian emission profiles also puts constraints on the shape and size of the illuminated volume [23],[24].

In this context, metal-coated micro-structured tapered optical fibers (μTFs) emerged as an effective system to deliver light to restricted brain volumes in superficial or deep brain areas. μTFs allow dynamic selection and modulation of light-emission properties [25]–[27], and the tapering reduces tissue damage. Light-emission can be restricted to small, micro-patterned apertures emitting light along directions tilted with respect to the taper surface [26]. This is endowed by the photonic properties of the taper itself, which modifies the transverse wavevector of guided modes, generating light emission angles that would otherwise require the inclusion of light-redirecting elements [2],[28]–[30]. However, adding extracellular recording electrodes on the curved taper edge represents a significant

Europe PMC Funders Author Manuscripts

technological challenge, because the small radius of curvature is incompatible with standard micro and nanofabrication planar techniques [31].

We present a new design concept – the "fibertrode" – integrating microelectrodes on a tapered optical fiber (TF). The microelectrodes are placed very close (10 μm) to the light emitting sites, yet the peculiar photonic properties of the taper, combined with novel fabrication strategies, eliminate photoelectric artefacts during optogenetic light trains. The taper acts upon the guided-mode wavevector to tilt the illumination pattern with respect to the fibertrode axis, thus preventing direct illumination of the electrode, as computationally confirmed by Monte Carlo simulations. The volume of stimulated tissue can be adjusted by changing the size and shape of the optical window, and electrodes with different sizes enable impedance tuning. High-resolution patterning techniques are employed to structure the non-planar surface of the taper, including: (i) focused ion beam (FIB) processing to realize a single electrode/window pair, and (ii) non-planar two-photon polymerization (2PP) to scale up the approach. When applied to the taper edge, 2PP allows all-optical patterning of a surface with non-constant radius of curvature, enabling multiple electrodes to be placed around the implant, with almost arbitrary patterns and customizable light emission geometries. We first tested fibertrodes *in vitro* to characterize photoelectric artefacts, then we performed electrophysiological recordings *in vivo* in the cerebral cortex and striatum of the mouse brain, demonstrating spatially confined optogenetic activation and simultaneous artefact-free extracellular recording of local field potentials (LFPs) and action potentials. Results confirm that the angled emission allows simultaneous optogenetic activation and electrical readout of neural activity over small brain areas, without need for post-hoc correction of photo-induced electrical artefacts. Therefore, fibertrodes represent a powerful tool for monitoring and modulating local neural networks simultaneously.

High resolution patterning of tapered fibers non-planar edge

A key challenge in fabricating integrated fibertrodes based on TFs is structuring the non-planar surface of the taper, whose radius of curvature $r(x)$ decreases along the waveguide axis x (definitions in Figure 1a). This configuration requires: (i) conformal deposition methods for insulating and metallizing a conical waveguide; (ii) patterning techniques with high positioning accuracy and spatial resolution much smaller than $r(x)$. We investigated two alternative patterning techniques (Figure 1). The first one is based on FIB milling and induced deposition (IBID), which allows high resolution and it was employed to develop the fibertrodes operating principles. To scale up the approach and overcome the main limitations of FIB-based fabrication, we developed a novel system, exploiting two-photon polymerization to build non-planar patterns on the taper edge, aimed at multiple extracellular recording sites along and all-around the waveguide.

Figure 1a illustrates the FIB-based method: two aluminum (Al) layers were alternated by two Parylene-C (Prl-C) insulating films, obtaining a metallic-confined waveguide [32] [33] that prevents light to impinge on the upper Al layer [34]. A 1 μm-thick Prl-C film was then conformally deposited, insulating the Al layer [35]. The second Al layer was evaporated without rotating the fiber, covering only one side of the waveguide, serving as an electrical path for the microelectrode. Apertures for outcoupling light were then obtained

Europe PMC Funders Author Manuscripts

Europe PMC Funders Author Manuscripts

by FIB milling through the Al/Prl-C/Al stack [36]. This exposes the two Al layers along the window's sidewalls, sealed again with a second Prl-C layer. Next, the shallow Prl-C insulation was locally removed with FIB milling to expose the Al layer, and Platinum (Pt) was deposited in the recess by IBID, scanning the ion beam on a circular surface slightly bigger than the recess, with deposition parameters optimized to maximize texture homogeneity [34] (final device configuration in Figure 1b).

To increase the number of recording sites and to pattern the waveguide all around the optical axis, we developed the 2PP-based approach. The TF is submerged in negative-tone photoresist and mounted on a 4–axis piezoelectric system using a custom holder (Figure 1c) allowing for moving and rotating the TF. The laser beam is moved by means of a galvanometric mirror scan head, and the TF roto-translates to build a resist mask. Although the photo-initiation reaction is independent from the surface curvature radius, since it takes place in a confined volume (voxel) into the photoresist, the curved surface of the TF places constraints on the minimum radius of curvature that can be patterned (R^{min}), which should be large enough to contain the entire voxel on the curved surface. We set a voxel size to obtain R^{min}~1.5 μm (details in Supplementary Figure 1), enabling fabrication of resists masks all around and along the entire taper (Figure 1c). Electrode patterns comprising contact pads, electrode traces and connection pads can therefore be realized by 2PP on metal-coated TFs and subsequent wet etching and resist removal (Figure 1d). After a Prl-C coating, the measurement pads are exposed by a recess and a platinum layer is deposited (Figure 1e).

Electrical properties of fibertrodes

Electrodes' impedances were measured by Electrochemical Impedance Spectroscopy after bonding the probe to a printed circuit board (PCB, see Methods and Supplementary Figure 2). Figure 2a and 2b show the electrodes morphology and the measured Bode plots. The typical constant phase element response was observed [37][38], independently from the electrodes' size, with phase close to -70° in the frequency range 100 Hz -10 kHz, while magnitude was higher in electrodes with lower surface area [39]. Data related to 2PP highlight the reproducibility of the fabrication process (1.32±0.92 MΩ/-75.56° ±3.18° magnitude/phase, mean±standard deviation at 1 kHz, n=7 probes, 15 μm-diameter electrode). Full frequency range measurement are displayed in Supplementary Figure 3 for 2PP and FIB electrodes, showing a slight deviation in phase below 10 Hz and a slightly higher variability across the 2PP probes (n = 7) compared with the FIB ones (n = 6), probably due to the soldering to the PCB.

In vivo broadband recordings of spontaneous neural activity in the 300 Hz-10 kHz band in layer 2/3 (L2/3) somatosensory cortex of C57BL/6 mice revealed extensive neural spiking (Figure 2c). Offline waveform analysis of action potentials identified up to three clustered waveforms acquired with both FIB and 2PP probes (Figure 2d and 2e, respectively; $L\text{-}ratio \leq 0.06$), validating fibertrodes for neuronal action potentials *in vivo* recordings.

We recorded LFPs (1-100 Hz) in layer 5 (L5) of Thy1-ChR2 transgenic mice somatosensory cortex, using the configuration in Figure 2f (details in Methods). A fibertrode featuring two

Europe PMC Funders Author Manuscripts

Europe PMC Funders Author Manuscripts

recording pads (Ch1 and Ch2) spaced ~550 μm was tested with Ch1 in L2/3 and Ch2 in L5 (Figure 2g). The root mean square (RMS) noise of the recorded signal was <10 μV for both channels and enabled independent measurement of spontaneous activity and spike sorting of action potentials (principal component analysis (PCA) displayed in Figure 2h). A summary of the quality metrics for PCA analysis is reported in Supplementary Table 1.

Optical properties

Light-emission patterns from FIB-milled windows of varied dimensions were characterized (Figure 3a,b). Light was launched into the fiber with a specific input angle θ_{in}~24°, which maximized the output power (Figure 3c,d) for windows fabricated at a diameter of ~90μm [26][32]. 2 mW input into the taper resulted in average output power density of 0.5 - 0.8 mW/mm^2. Importantly, the emitted light forms an angle θ_{OUT} ~ 24°, independently from the windows' size (Figure 3d), with respect to the taper axis, resulting in a directional emission that we exploited to reduce direct illumination of the recording pad. The amount of illumination received by the electrode was estimated by Monte Carlo simulations modeling local light scattering (details in Methods) [40] [41]. Figure 3e shows three-dimensional iso-intensity surface maps of the simulated emission patterns, with top and side views in Figure 3f. The power-density distributions around the apertures were minimized above the optical window, and a second region with low photon counts can be identified also just below the aperture. The simulations suggest that the window size can be engineered to obtain the optimal stimulated volume for a specific application and help in identifying the electrode(s) position that minimizes direct illumination. From our simulations the stimulated tissue volume can be tailored from ~10^{-5} to ~10^{-3} mm^3 by changing the emitted power density from 1 mW/mm^2 to 8 mW/mm^2 for windows of 20×20 μm^2, 40×40 μm^2, and 60×60 μm^2 (Supplementary Figure 4). Assuming a density of $3{\cdot}10^4$ neurons/mm^3 in mouse cortex [42], these volumes include from some to a few tens of neurons.

Photoelectric response

Stacked metal layers could be a source of photoelectric artefacts, due to light interaction with the inner layer. In a metallic-confined waveguide, propagating and evanescent modes generate a surface current density on the metallic cladding [43], potentially giving rise to spurious electrical signals. Moreover, electric currents can be generated by multi-photon absorption of 473 nm light [13]. To characterize photo-induced artefacts, we immersed fibertrodes (window-electrode distance 10 μm) in Phosphate Buffered Saline solution (PBS) applying trains of 2 mW/mm^2 light pulses of 2 ms or 100 ms at 473 nm, recording voltage changes. The double Al/Prl-C stack fibertrode showed a small light-dependent voltage change in the low-frequency band (LF: 3-250 Hz) for 100 ms pulses and no artefacts in the high-frequency band (HF: 0.25-10 kHz) for both investigated pulse duration (Figure 4a).

Since light interaction with the electrode is avoided by the relative window-electrode placement, the LF artefact for long light pulses could arise from light interaction with the internal layer, generating a current in the external Al layer through capacitive coupling, due to the wide overlapping surfaces of the two Al layers. To confirm this, we tested a probe with no optical window (Figure 4b), finding artefacts comparable with the ones for

Europe PMC Funders Author Manuscripts

Europe PMC Funders Author Manuscripts

the windowed probe, although the inner Al layer should effectively shield the outer one (light interaction with the metal was maximized by injecting 100 ms light pulses into the entire fiber numerical aperture). Importantly, when the laser pulse was reduced to 2 ms, LF artefacts were not detectable (Figure 4a). Therefore the FIB-based design shows a marked reduction of HF photo-electrical artefact with a residual LF photoelectric signal detected only for long light pulses.

To minimize also LF artefacts, we substituted the external metal layer with a 10 μm-large electric track built by the 2PP method. The first test configuration consists of a single recording pad above the optical window, and related time traces show neither HF nor LF artefacts with long or short stimulation pulses (Figure 4c and Supplementary Figure 4). The second one consists of a 500 μm slot aperture, and recording sites at the top (Ch1) and bottom edges (Ch2), to demonstrate that: (i) the 2PP technique enables the realization of multiple electrodes, and (ii) light-emission directionality can be exploited to reduce photoelectric noise both above and below the emitting window. By changing θ_{in}, illumination can be redistributed along the slot (Supplementary Figure 4). Both Ch1 and Ch2 show no HF or LF artefacts emerging from the baseline noise (injection optical paths in Supplementary Figure 5). In addition, the low artifact operation is preserved at multiple wavelenghts (Supplementary Figure 6).

In vivo experiments

Fibertrodes were employed for optogenetic stimulation and simultaneous electrical monitoring of neural activity, in the striatum of awake *Adora2a-Cre;Ai32* mice, expressing Channelrhodopsin2-EYFP (ChR2) in striatal spiny projection neurons of the indirect pathway.

473 nm laser light (output power density of 0.4-10 mW/mm^2) induced robust firing of action potentials in neighboring neurons. Neural stimulation was effective with all window sizes tested (see representative data in Figure 5a and Supplementary Figure 7), with the 60×60 μm^2 window resulting in higher spiking activity, due to larger activation volume (Figure 3e).

To address whether fibertrodes can drive temporally precise action potentials we performed recordings of neural activity in L5 somatosensory cortex of Thy1-ChR2 mice. Compared to striatal SPNs, L5 pyramidal cells have faster spiking kinetics, which enables better characterization of the temporal properties of fibertrode optogenetic stimulation. Short 2 ms optical pulses were delivered in either a fibertrode featuring two electrodes above and below a 500 μm-long slot aperture, or a single electrode and single window (Figures 5d,e,f and 5g,h,i). Optically-evoked spikes had latencies in the intervals 1–2 ms, 4–5 ms and 7–8 ms, with respect to the light onset (Figure 5e,f and Figure 5h,i), consistent with previous observation [16]. The RMS noise <15 μV (mean value estimated on a total of 10 recordings) enabled putative spike sorting of light-triggered action potentials (Supplementary Figure 5).

Large LFP deflections were elicited by 473 nm light pulses (duration 5 ms at ~10 mW/mm^2, Supplementary Figure 7), indicating the capability to recruit large neuronal ensembles when

used at higher light-power. Despite this strong activation we did not detect LFP optical artefacts, in agreement with control experiments in Figure 4.

Scalability of the approach

The use of 2PP to pattern the taper edge enables the realization of arbitrary electrodes patterns and light-delivery geometries around the implant axis, an approach only possible with the technology presented in this work. This overcomes the intrinsic limitation of the FIB-based fabrication, which is practical for prototyping, but requires a pair of metal/insulating layers for each additional electrode, introducing capacitive crosstalk. The versatility of 2PP relies on the ability to pattern the waveguide along and around the entire taper surface, despite its non-constant radius of curvature.

Example configurations are shown in Figure 6a-b, including: multiple electric tracks in a spiral geometry and a tetrode design on the non-planar taper edge. Remarkably, 2PP allows realizing both light delivery patterns and extracellular recording electrodes with 2PP processes followed by metal lift-off and wet etching (see detailed steps in Supplementary Figure 8). This is shown for the slot-emitting device featuring two recording pads displayed in Figure 6c (already tested in vitro and in vivo in Figure 4d and 5d-f), and for a device featuring two recording pads coupled with two optical windows (Figure 6d). Importantly, the last two steps in Supplementary Figure 8 can be sped up by using 2PP to insulate the electrical tracks apart from the connection and measurement pads, thus defining the area for subsequent electrochemical deposition.

Cost-effectiveness can be improved by: (i) metal/parylene stacks made in parallel on tens of fibers; (ii) wet-etching steps performed in parallel on tens of devices; (iii) 2PP sped up with production-ready machines hundreds of times faster (for instance Nanoscribe, GmbH), and with multi-beam holographic lithography [44]. These processes have the advantage of not requiring a foundry for semiconductor manufacturing, which increases the cost of a single device unless this is intended for mass production. We expect the unit cost of fibertrodes to be lower than other type of optrodes based on μLEDs or ridge waveguide technology.

Outlook

We show that the photonic properties of tapered “fibertrodes” enable artefact-free extracellular recordings during optogenetic stimulation of spatially confined neuronal populations. Metal coated TFs allowed the integration of extracellular Pt electrodes near light-emitting sites. The effect of the taper on modal propagation generates an angled emission that minimizes light incidence on the electrode, largely abating direct illumination photoelectric artefacts.

The fibertrode allowed reliable optogenetic activation and electrophysiological recording of ChR2-expressing neurons in both the striatum and the cortex. By tailoring window and electrode sizes as well as their reciprocal position, fibertrodes can stimulate tissue volumes ranging from 10^{-5} mm^3 to 10^{-3} mm^3 (Figure 3e). Thus, fibertrodes offer the unprecedented possibility of spatially confining optogenetic stimulation to very restricted neuronal populations, while recording electric neuronal responses. The ability to work

Europe PMC Funders Author Manuscripts
Europe PMC Funders Author Manuscripts

Europe PMC Funders Author Manuscripts

Europe PMC Funders Author Manuscripts

on very small volumes and at multiple wavelengths, suggests that fibertrodes can be a promising technology for opto-tagging [45], which can exploit both excitatory and inhibitory opsins, these latter being activated at red-shifted wavelengths. Inhibitory opsins are indeed more efficient to identify specific cellular populations, since ChR2 light-driven modulation latencies are often comparable with synaptic delays, making indistinguishable ChR2+ and ChR2-responses [46]. Competing technologies are limited in terms of multi-wavelength operation and small volume excitation. For example, μLEDs Lambertian emission can put constrains to electrode-emitter distances [23,24], with best recorded artefacts of ~50 μV peak-to-peak for heavily boron-doped silicon substrate with time resolution below 1 ms [22]. Artefacts in μLEDs technology can be also assigned to coupling across integrated electrical channels, and can be removed by noise-reduction algorithms [21], while flat-cleaved optical fibers have a wide emitting surface that necessarily generates a larger excited volume (~$7{\cdot}10^{-3}$ mm^3 [25]), also at low power density of 2 mW/mm^2. Moreover, the highly localized, patterning versatility and scalability introduced by the 2PP methodology allows for fabricating probes with customized electrodes positions and light emission patterns along and around the taper, exploiting the entire surface of the device around the implant axis. This could also be employed to design fibertrodes exploiting tetrodes-like configurations, to improve sorting quality when trying to cluster multiple units. This level of high-resolution conformal patterning on non-planar surfaces has not been demonstrated yet for transparent conductive materials like ITO, PEDOT or graphene, previously suggested to reduce photoelectric artefacts [13]. The fibertrode's optical window can be engineered to illuminate specific brain volumes, and the impedance of the Pt electrodes can be controlled by changing its surface area, even if fabricated on a highly non-planar fiber surface.

The design concepts introduced here can be extended to the combination of wide-volume optical control and simultaneous LFP recordings from a single recording site. In this case, light could impinge on the electrode, causing electric artefacts. A configuration that solves this problem is schematized in Supplementary Figure 9: a recording site is placed just above the first emission diameter of the TF, shielded from internal irradiation by the fiber cladding, which is preserved along the taper of 0.66 NA borosilicate-glass fibers [26]. In Supplementary Figures 9 representative *in vitro* recordings in both HF and LF band show no photoelectric artefacts even with 100 ms light pulses. With this dielectric shielding, current density induced by propagating and evanescent modes does not arise because the confinement is purely dielectric. Although not shown in this work, the ability to act on the stimulation site on either small or wide volumes, together with HF and LF recordings, would support the further development of implantable devices for real time feedback in combined optical stimulation/electrical readout experiments. [47], [48].

Overall, the fibertrode technology can drive new experiments for optogenetic investigation of brain circuits on small and customizable brain volumes, enabling local recording of neural activity. More complex optrode systems can also be designed by arranging multiple fibertrodes in customized arrays featuring peculiar electrodes patterns and on-demand light emission geometries.

Europe PMC Funders Author Manuscripts

Europe PMC Funders Author Manuscripts

Methods

Animals

Experimental manipulations on mice were performed in accordance with protocols approved by: (i) the Harvard Standing Committee on Animal Care and guidelines described in the US National Institutes of Health *Guide for the Care and Use of Laboratory Animals*; (ii) Italian Ministry of Health. For electrophysiological recordings in striatum *Adora2a*-Cre transgenic mice (GENSAT #KG139Gsat) were bred to conditional channelrhodopsin-2 (ChR2) expression; mice expressing ChR2(H134R)-EYFP under control of an upstream *loxP*-flanked STOP cassette (Ai32; referred to as *ChR2*$^{f/f}$; The Jackson Laboratory #012569). Electrophysiological recordings in cortex were performed in Thy1-ChR2-YFP mice (The Jackson Laboratory #007612). In all the experiments, male and female mice were used. All used animals were 6-8 weeks old, housing conditions: 12 hour light-dark cycle, 22-24°C and 20/55% humidity.

Brain tissue processing and imaging

Recording locations were confirmed post hoc by whole brain sectioning and imaging. After recordings mice were deeply anesthetized with isoflurane and perfused transcardially with 4% paraformaldehyde in 0.1 M sodium phosphate buffer. Brains were fixed for 24 h at 4 °C, washed in phosphate buffer saline (PBS) and sectioned (100 μm) coronally using a vibratome (Leica VT1000s). Brain sections were mounted on glass slides, dried and mounted with ProLong antifade reagent containing DAPI (Molecular Probes). Whole brain sections were imaged with an Olympus VS110 slide-scanning microscope.

Surgeries and in vivo recordings

For experiments shown in Figure 2c-f, Figure 5a-c, Supplementary Figure 6 animals were anesthetized with isoflurane and placed in a stereotaxic apparatus. After surgical removal of scalp and cleaning of the skull with saline and 70% ethanol, two craniotomies were made with a 0.5-mm burr micro drill at (AP - 0 mm; ML - 2.0 mm and AP - 0.3 mm; ML - +1.5 mm from Bregma) and sealed with Kwik-Cast silicone Elastomere. Animals were fitted with a custom-made titanium head bar using transparent glue (Loctite 454) and allowed to recover from anesthesia for 1 h on a heat pad at 38 °C. Following recovery from anesthesia, animals were head fixed and *in vivo* electrophysiological recordings were performed using different fibertrodes.

Cortical recordings in L5 were done by positioning the electrode/window 1,250 μm deep from the brain surface, whereas striatal recordings were performed at a 2,500 - 2,750 μm depth. Optogenetic stimulation was achieved by coupling a 200 μm core optical fiber (Thorlabs FT200UMT, 0.39 NA) using a 473 nm laser source. Light pulses were controlled with an Acousto-Optic Modulator (AA Opto-Electronic) for fast shuttering and intensity control. Final light power was 2 mW at the patch cord and pulse width was set depending on the specific experiment (details reported in the main text, Figures and their captions). All recordings were validated by post hoc serial histological analysis of electrode placement. For LFP experiments in Figure 2f, light was delivered extra-cranially with a 200 μm-core optic fiber over the *dura mater* near the fibertrode implant. Optogenetic stimulation (488nm laser

Europe PMC Funders Author Manuscripts

Europe PMC Funders Author Manuscripts

light, 2 mW or 20 mW) was used to activate L5 pyramidal neuron dendrites that extend to superficial cortical layers, eliciting robust LFPs time-locked to the light pulses (Figure 2f).

For experiments shown in Figure 2g, e, h, Figure 5d-i and Supplementary Figure 6 mice were anesthetized with Avertin and craniotomies performed under a stereotaxic apparatus. After surgical removal of the scalp the dura mater was also removed and L5 of somatosensory or motor cortex have been addressed at implant depths depending on the used fibertrode design. More in detail, mouse 1 (wild type) was used for data in Figure 2c,d,f; mouse 2 (wild type) was used for data in Figure 2e; mouse 3 (wild type) was used for data in Figure 2g,h; mouse 4,5,6 were used for data in Figure 5b,c, Supplementary Figure 6a,b,c,f,g; mouse 7 was used for data in Figure 6e,f and Supplementary Figure 6d; mouse 8 was used for data in Figure 5h,i and Supplementary Figure 6e; mouse 9 (wild type) was used for data in Figure 5h (control trace) and mouse 10 (wild type) was used for data in Supplementary Figure 6h.

Data acquisition and analysis

For electrophysiology recordings of *in vivo* neural activity shown in Figure 2c,d,f, Figure 5b-c, Supplementary Figures 6, extracellular signals were amplified and band-pass filtered (300 Hz – 10 kHz) using a A-M Systems Model 1800 microelectrode AC amplifier (A-M Systems) and digitized at 40 kHz using a NI-DAQ 6363 acquisition board (National Instruments) and a custom version of ScanImage written in MATLAB (MathWorks). Off-line analysis of light evoked action potentials was performed using custom routines written in MATLAB. Spike sorting depicted in Figure 2 was performed via PCA in Offline Sorter v4 (Plexon Inc.). For experiments shown in Figure 2e,g,h, Figure 5d-i and Supplementary Figure 6 PCBs were connected to an RHD 16 channels Intan head-stage connected via an SPI cable to a PZ5 multi-modal NeuroDigitizer (Tucker and Davis ltd.). Data were acquired at 20 kHz through a RZ2 bioamp processor and visualized in real time on Synapse software. Extracellular signals were amplified and band-pass filtered (300 Hz – 10 kHz). Signal to noise ratio (SNR) was calculated as $SNR = \sigma^2_{Signal}/\sigma^2_{Noise}$, where σ^2_{Signal} and σ^2_{Noise} were extracted from all the samples within and outside the extracted spikes, respectively. Noise floor was defined $\sqrt{\sigma^2_{Noise}}$. For *post-hoc* data analysis, spike sorting and quality metrics calculations, custom MATLAB routines for signal processing and Offline Sorter v4 software were used. Waveform detection was performed setting a detection threshold ranging from 4 to 5 times the standard deviation of the noise and aligned by global minimum between sort start/stop times (1.5 ms). PCA was performed on the total pool of aligned waveforms. *L-ratio* and *isolation distance isoD* have been used as metrics for *per-unit* sort quality estimation, as per Ref.[10], [49]–[51] and have been calculated by Offline Sorter v4. Cluster cutting ellipses showing a 95% confidence level of the clustered data have been calculated with custom MATLAB code. Supplementary Table 1 summarizes relevant recording systems settings and obtained quality metrics in PCA analysis.

FIB-based Fibertrode fabrication process

The optrode is based on an optical fiber (0.39 NA FT200UMT, Thorlabs) with one of the ends tapered down to a sub-micrometer tip with a low angle over a length of few millimeters. Tapered fibers were realized by the heat and pull method as described in [34].

Europe PMC Funders Author Manuscripts

Europe PMC Funders Author Manuscripts

An Al/Prl-C/Al stack (Figure 1A) is deposited onto the taper by alternating metal thermal deposition and insulator physical vapor deposition (STS Coating System). The fiber is kept under rotation during the first Al deposition to obtain metallization over the entire taper surface, with the fiber tip slightly tilted toward the crucible, resulting in a ~200 nm-thick coating. The second Al layer is instead deposited without rotation of the fiber covering approximately half of the taper surface. Localized removal of the deposited materials to realize a squared optical aperture (Figure 1B) is obtained by Focused Ion Beam milling (FEI® Helios™ NanoLab™ 600i DualBeam™, equipped with the Tomahawk FIB column). An insulated metallic wire with uninsulated ends is glued with a conductive epoxy to the metallized portion of the fiber a few millimeters apart from the tapered region. A second Prl-C layer is then deposited for final insulation of the probe. This process will also encapsulate the metal exposed at the optical window sidewalls during milling. Finally, the microelectrode is realized by FIB milling of the second Prl-C to expose the second deposited Al layer followed by Ion Beam Induced Deposition (IBID) of platinum to fabricate a circular microelectrode, at a rate of ~0.45 $\mu m^3/s$. Electrode is connected to the PCB by an insulated copper wire fixed at the external Al layer by means of Ag paste.

2PP-based Fibertrode fabrication process

Tapered fibers were realized by the heat and pull method as described in [34] from 0.22 NA fibers (FG200LEA, Thorlabs), and from 0.66 NA fibers (Plexon PlexBright High Performace patch cable). The tapers were then mounted via a custom holder on a 4-axis piezoelectric stage (Physik Intrumente Q-545 Q-Motion for *x*, *y* and *z*, Physik Instrumente U-628 PIline for the rotation around the fiber axis) and inserted in a 3D-printed PDMS tank, filled with IP-S 780 photoresist (Nanoscribe, GmbH).

After the first 2PP process (voxel sizes were of $d_{x,y}$ ~ 500 nm in the (*x*,*y*) plane and d_z ~ 3 μm along the *z* axis), polymeric masks are impressed on the dielectric fiber. Continuously rotating the fiber during a thermal evaporation process would result in covering also the 2PP masks, making it difficult to remove them after the deposition, to obtain optical apertures on the TF. For this reason, TFs with 2PP masks undergo a three-staged thermal evaporation process, aimed at leaving uncovered a certain gap (typically 1 μm) to facilitate mask removal. The fiber is subjected to a first evaporation with the 2PP masks facing directly the crucible, and two other steps setting an angle between the normal to the mask and the metal flux direction given by:

$$\theta\,(^\circ) = \cos^{-1}\left(\frac{R - h_{gap}}{R}\right) + \sin^{-1}\left(\frac{1}{2R}\right) + 90,$$

where *R* is the TF radius at a certain section, *l* is the lateral size of the 2PP mask along the transversal direction, and h_{gap} is the height of the gap that has to remain uncovered (typically, 1 μm). After the 2PP mask removal apertures as shown in Supplementary Figure 7.

Devices equipped with optical apertures were subjected to a conformal evaporation of a 1 μm-thick Prl-C layer, followed by electron beam evaporation of a 200 nm-thick gold (Au)

Europe PMC Funders Author Manuscripts

Europe PMC Funders Author Manuscripts

layer, plus a 5 nm-thick Chromium adhesion layer, while the fibers were kept in rotation thanks to a stepper motor. A 2PP process allows to obtain a polymeric mask anchored to the gold-coated TF's surface (Figure 1D), protecting the underneath gold from chemical wet etching of gold (Sigma-Aldrich Gold etchant, standard) and of chromium (Sigma-Aldrich Chromium etchant). The 2PP mask is removed by soaking the fiber in H_2SO_4:H_2O_2 3:1 solution and rinsing it in de-ionized H_2O.

TFs with metallic patterns are connected to a custom 3D printed PCB (Supplementary Figure 2) and insulated by a second conformal evaporation of a 1 μm-thick Prl-C layer. A combination of FIB milling and IBID (Figure 1E) is used, respectively, to remove the Prl-C from the measurement pad (definition in Figure 1D) and to tune the electrode impedance by Pt deposition into the recess. The complete process is schematized in Supplementary Figure 7.

Electrochemical Impedance Spectroscopy

Electrochemical Impedance Spectroscopy (EIS) was performed with a commercially available potentiostat system (ZIVE SP1, WonAtech Co., LTD.). Measurements were taken in Phosphate Buffered Saline solution (PBS) in the three electrodes configuration, with the fabricated microelectrode, a silver chloride wire and a platinum wire immersed acting as the working electrode, the reference electrode and the counter electrode, respectively. Potentiostatic sinusoidal waveforms (10 mV rms, 1 Hz - 100 kHz) were applied with respect to the open-circuit potential (OCP) in order to let the actual surface conditions of the microelectrodes drive the measurement results.

Light emission and artefacts characterization

Light emission properties were assessed by injecting 473 nm laser (Laser Quantum Ciel 473) into the optrode at different angles through a galvanometric mirror based scanning system as described in [26]. Optrodes were immersed in 30 μM Fluorescein:PBS solution and light emission images were acquired using a fluorescence microscope (Scientifica Slicescope, 4X objective Olympus XLFLUOR4X/340 with immersion cap XL-CAP; sCMOS Hamamatsu ORCA-Flash4.0 V2 camera). Images were acquired for all fibertrodes. For each different input angle, optical output power was measured in air by placing the optical window near to a Thorlabs PM100USB power meter with S120VC sensor head. Power coupling efficiency was measured as the ratio between taper and patch fiber optical power output while power density was calculated as the ratio between the emitted light power and the window area ($20 \times 20\ \mu m^2$, $40 \times 40\ \mu m^2$ or $60 \times 60\ \mu m^2$, and $500 \times 20\ \mu m^2$ for the slot aperture).

Devices were tested in PBS solution for light artefacts and electrical noise. 473 nm light (Laser Quantum Ciel 473) was injected as displayed in Figure 4. Electrodes were connected to a 32-channel amplifier board (RHD2164 64-Channel Amplifier Board) and electrical recordings were performed using an Axon™pCLAMP™ Data Acquisition System and an Intan RHD2000 breadboard (20 kHz sampling rate). pClamp software is used to trigger light stimulus delivered by 473 nm laser connected to one of the breadboard ADC channels, while the electrode is connected via a male connector to one of the head-stage channels. Data

obtained by injecting laser light at a wavelength of 594 nm (Obis, Coherent GmbH) are reported in Supplementary Figure 9.

Monte Carlo simulations of light propagation

Light emission patterns in tissue of window and slot apertures were simulated with a Monte Carlo MATLAB code based on the one proposed in [40]. Starting positions and propagation directions of emitted photons were changed to match the properties of the apertures realized on the tapered fiber reported in the main text. Light scattering parameters provided by the original code were employed. 1000 packets of $1{\cdot}10^5$ photons were generated from a uniform distribution in the ranges $\theta_{OUTmin,xz} < \theta_{OUT,xz} < \theta_{OUTmax,xz}$ and $-\Delta\theta_{OUT,xy}/2 < \theta_{OUT,xy} < \Delta\theta_{OUT,xy}/2$ in the (x,z) and (x,y) planes, respectively (Figure 3c for definitions). Brain tissue was modeled with a Henyey-Greenstein scattering function, with parameters $n = 1.360$, $l = 90.16$ μm, $g = 0.89$, $T = 0.9874$.

Supplementary Material

Refer to Web version on PubMed Central for supplementary material.

Acknowledgements

B.S., A.B., M.B., Fi.P. and Fe.P. acknowledge funding from the European Research Council under the European Union's Horizon 2020 research and innovation program (#677683); M.P. and M.D.V. acknowledge funding from the European Research Council under the European Union's Horizon 2020 research and innovation program (#692943). M.B., M.D.V. and F.P. acknowledge funding from the European Research Council under the European Union's Horizon 2020 research and innovation program (#966674). Fi.P., M.D.V. and Fe.P. acknowledge that this project has received funding from the European Union's Horizon 2020 Research and Innovation Program under Grant Agreement No 101016787. L.S., M.D.V. and B.L.S. are funded by the US National Institutes of Health (U01NS094190). M.P., L.S., Fe.P., M.D.V., B.L.S. are funded by the US National Institutes of Health (1UF1NS108177-01). A.B., Fe.P. and M.D.V. also acknowledge funding from the European Union's Horizon 2020 research and innovation program under grant agreement (#828972). Authors also acknowledge Jaeeon Lee for help setting up the optrode fiber launch system.

Data Avaibility Statement

The datasets generated during and/or analyzed during the current study are available from the corresponding author on reasonable request and are available on the Zenodo repository (DOI 10.5281/zenodo.6477861). Data on optrode fabrication and in vitro optical measurements are available from B.S., A.B., L.S., Fe.P. and M.D.V. Data on in vivo use of tapered fibers are available from B.S., R.P., B.L.S. and Fe.P.

Code Avaibility Statement

The scripts related to Monte Carlo simulations used in the current study are available from the corresponding author on reasonable request and are available on the Zenodo repository (DOI 10.5281/zenodo.6477861).

References

[1]. Camporeze B, et al. Optogenetics: the new molecular approach to control functions of neural cells in epilepsy, depression and tumors of the central nervous system. Am J Cancer Res. 2018; 8 (10) 1900–1918. [PubMed: 30416844]

Europe PMC Funders Author Manuscripts

Europe PMC Funders Author Manuscripts

Europe PMC Funders Author Manuscripts

Europe PMC Funders Author Manuscripts

[2]. Grosenick L, Marshel JH, Deisseroth K. Closed-loop and activity-guided optogenetic control. Neuron. 2015; 86 (1) 106–139. [PubMed: 25856490]

[3]. Segev E, et al. Patterned photostimulation via visible-wavelength photonic probes for deep brain optogenetics. Neurophotonics. 2016; 4 (1) 11002

[4]. Zorzos AN, Boyden ES, Fonstad CG. Multiwaveguide implantable probe for light delivery to sets of distributed brain targets. Opt Lett. 2010; 35 (24) 4133–4135. [PubMed: 21165114]

[5]. Wu F, et al. An implantable neural probe with monolithically integrated dielectric waveguide and recording electrodes for optogenetics applications. J Neural Eng. 2013; 10 (5) 56012

[6]. Deubner J, Coulon P, Diester I. Optogenetic approaches to study the mammalian brain. Curr Opin Struct Biol. 2019; 57: 157–163. [PubMed: 31082625]

[7]. Nakamura T, et al. Increased intracellular Ca2+ concentration in the hippocampal CA1 area during global ischemia and reperfusion in the rat: a possible cause of delayed neuronal death. Neuroscience. 1999; 88 (1) 57–67. [PubMed: 10051189]

[8]. Bradley PMJ, Murphy D, Kasparov S, Croker J, Paton JFR. A micro-optrode for simultaneous extracellular electrical and intracellular optical recording from neurons in an intact oscillatory neuronal network. J Neurosci Methods. 2008; 168 (2) 383–395. [PubMed: 18155773]

[9]. LeChasseur Y, et al. A microprobe for parallel optical and electrical recordings from single neurons in vivo. Nat Methods. 2011; 8 (4) 319–325. [PubMed: 21317908]

[10]. Anikeeva P, et al. Optetrode: a multichannel readout for optogenetic control in freely moving mice. Nat Neurosci. 2012; 15 (1) 163–170.

[11]. Kim EGR, et al. 3D silicon neural probe with integrated optical fibers for optogenetic modulation. Lab Chip. 2015; 15 (14) 2939–2949. [PubMed: 26097907]

[12]. Sileo L, et al. Tapered fibers combined with a multi-electrode array for optogenetics in mouse medial prefrontal cortex. Front Neurosci. 2018; (12) 771. [PubMed: 30416424]

[13]. Kozai TDY, Vazquez AL. Photoelectric artefact from optogenetics and imaging on microelectrodes and bioelectronics: new challenges and opportunities. J Mater Chem B. 2015; 3 (25) 4965–4978. [PubMed: 26167283]

[14]. Kampasi K, et al. Dual color optogenetic control of neural populations using low-noise, multishank optoelectrodes. Microsystems Nanoeng. 2018; 4 (1)

[15]. Park S, et al. One-step optogenetics with multifunctional flexible polymer fibers. Nat Neurosci. 2017; 20 (4) 612. [PubMed: 28218915]

[16]. Lee J, Ozden I, Song Y-K, Nurmikko AV. Transparent intracortical microprobe array for simultaneous spatiotemporal optical stimulation and multichannel electrical recording. Nat Methods. 2015; 12 (12) 1157 [PubMed: 26457862]

[17]. Aravanis AM, et al. An optical neural interface: in vivo control of rodent motor cortex with integrated fiberoptic and optogenetic technology. J Neural Eng. 2007; 4 (3) S143. [PubMed: 17873414]

[18]. Yizhar O, Fenno LE, Davidson TJ, Mogri M, Deisseroth K. Optogenetics in neural systems. Neuron. 2011; 71 (1) 9–34. [PubMed: 21745635]

[19]. Mohanty A, et al. Reconfigurable nanophotonic silicon probes for sub-millisecond deep-brain optical stimulation. Nat Biomed Eng. 2020; 4 (2) 223–231. [PubMed: 32051578]

[20]. Klein E, Gossler C, Paul O, Ruther P. High-density μLED-based optical cochlear implant with improved thermomechanical behavior. Neurosci Front. 2018; 12: 659.

[21]. Wu F, Stark E, Ku P-C, Wise KD, Buzsáki G, Yoon E. Monolithically integrated μLEDs on silicon neural probes for high-resolution optogenetic studies in behaving animals. Neuron. 2015; 88 (6) 1136–1148. [PubMed: 26627311]

[22]. Kim K, Vöröslakos M, Seymour JP, Wise KD, Buzsáki G, Yoon E. Artifact-free and high-temporal-resolution in vivo opto-electrophysiology with microLED optoelectrodes. Nat Commun. 2020; 11 (1) 2063 [PubMed: 32345971]

[23]. McAlinden N, et al. Thermal and optical characterization of micro-LED probes for in vivo optogenetic neural stimulation. Opt Lett. 2013; 38 (6) 992–994. [PubMed: 23503284]

Europe PMC Funders Author Manuscripts

Europe PMC Funders Author Manuscripts

[24]. Scharf R, Tsunematsu T, McAlinden N, Dawson MD, Sakata S, Mathieson K. Depth-specific optogenetic control in vivo with a scalable, high-density µLED neural probe. Sci Rep. 2016; (6) 28381 [PubMed: 27334849]

[25]. Pisanello F, et al. Dynamic illumination of spatially restricted or large brain volumes via a single tapered optical fiber. Nat Neurosci. 2017; 20 (8)

[26]. Pisanello M, et al. Tailoring light delivery for optogenetics by modal demultiplexing in tapered optical fibers. Sci Rep. 2018; 8 (1)

[27]. Pisano, F; , et al. Depth-resolved optical monitoring of neural activity in freely moving animals; International Conference on Transparent Optical Networks; 2020 July.

[28]. Pisanello, M; Pisanello, F; Sileo, L; De Vittorio, M. Photonic technologies for optogenetics; 2014 16th International Conference on Transparent Optical Networks (ICTON); 2014. 1–4.

[29]. Warden MR, Cardin JA, Deisseroth K. Optical Neural Interfaces. Annu Rev Biomed Eng. 2014; 16 (1) 103–129. [PubMed: 25014785]

[30]. Dufour S, De Koninck Y. Optrodes for combined optogenetics and electrophysiology in live animals. Neurophotonics. 2015; 2 (3) 1–14.

[31]. Kostovski G, Stoddart PR, Mitchell A. The optical fiber tip: an inherently light-coupled microscopic platform for micro-and nanotechnologies. Adv Mater. 2014; 26 (23) 3798–3820. [PubMed: 24599822]

[32]. Pisanello M, Della Patria A, Sileo L, Sabatini BL, De Vittorio M, Pisanello F. Modal demultiplexing properties of tapered and nanostructured optical fibers for in vivo optogenetic control of neural activity. Biomed Opt Express. 2015; Oct; 6 (10) 4014–4026. [PubMed: 26504650]

[33]. Pisanello F, et al. Multipoint-emitting optical fibers for spatially addressable in vivo optogenetics. Neuron. 2014; 82 (6) 1245–1254. [PubMed: 24881834]

[34]. Sileo L, Pisanello M, De Vittorio M, Pisanello F. Fabrication of multipoint light emitting optical fibers for optogenetics. Optical Techniques in Neurosurgery, Neurophotonics, and Optogenetics II. 2015; 9305 93052O

[35]. Song JS, Lee S, Jung SH, Cha GC, Mun MS. Improved biocompatibility of parylene-C films prepared by chemical vapor deposition and the subsequent plasma treatment. J Appl Polym Sci. 2009; 112 (6) 3677–3685.

[36]. Pisano F, et al. Focused ion beam nanomachining of tapered optical fibers for patterned light delivery. Microelectron Eng. 2018; 195: 41–49. [PubMed: 31198228]

[37]. Abouzari MRS, Berkemeier F, Schmitz G, Wilmer D. On the physical interpretation of constant phase elements. Solid State Ionics. 2009; 180 (14–16) 922–927.

[38]. Rocha PRF, et al. Electrochemical noise and impedance of Au electrode/electrolyte interfaces enabling extracellular detection of glioma cell populations. Rep Sci. 2016; 6 (1) 1–10.

[39]. Hazubski S, Soekadar SR, Hoppe H, Otte A. Neuroprosthetics 2.0. EBioMedicine. 2019; 48: 22. [PubMed: 31594748]

[40]. Stujenske JM, Spellman T, Gordon JA. Modeling the spatiotemporal dynamics of light and heat propagation for in vivo optogenetics. Cell Rep. 2015; 12 (3) 525–534. [PubMed: 26166563]

[41]. Maglie E, et al. Ray tracing models for estimating light collection properties of microstructured tapered optical fibers for optical neural interfaces. Opt Lett. 2020; 45 (14) 3856–3859. [PubMed: 32667302]

[42]. Steenland HW, McNaughton BL. Silicon Probe Techniques for Large-Scale Multiunit Recording. Anal Model Coord Multi-neuronal Act. 2015. 41–61.

[43]. Saleh, BEA, Teich, MC. Fundamentals of photonics. john Wiley & sons; 2019.

[44]. Baldacchini, T. Three-dimensional microfabrication using two-photon polymerization: fundamentals, technology, and applications. William Andrew; 2015.

[45]. Nieh EH, et al. Decoding neural circuits that control compulsive sucrose seeking. Cell. 2015; 160 (3) 528–541. [PubMed: 25635460]

[46]. Brown J, et al. Expanding the optogenetics toolkit by topological inversion of rhodopsins. Cell. 2018; 175 (4) 1131–1140. [PubMed: 30343901]

[47]. Stark E, Roux L, Eichler R, Senzai Y, Royer S, Buzsáki G. Pyramidal cell-interneuron interactions underlie hippocampal ripple oscillations. Neuron. 2014; Jul; 83 (2) 467–480. [PubMed: 25033186]

[48]. Pisanello F, Sileo L, De Vittorio M. Micro- and Nanotechnologies for Optical Neural Interfaces. Front Neurosci. 2016; 10: 70. [PubMed: 27013939]

[49]. Sigurdsson T, Stark KL, Karayiorgou M, Gogos JA, Gordon JA. Impaired hippocampal-prefrontal synchrony in a genetic mouse model of schizophrenia. Nature. 2010; 464 (7289) 763–767. [PubMed: 20360742]

[50]. Schmitzer-Torbert N, Jackson J, Henze D, Harris K, Redish AD. Quantitative measures of cluster quality for use in extracellular recordings. Neuroscience. 2005; 131 (1) 1–11. [PubMed: 15680687]

[51]. Dhawale AK, Poddar R, Wolff SBE, Normand VA, Kopelowitz E, Ölveczky BP. Automated long-term recording and analysis of neural activity in behaving animals. Elife. 2017; 6 e27702 [PubMed: 28885141]

Europe PMC Funders Author Manuscripts

Europe PMC Funders Author Manuscripts

Europe PMC Funders Author Manuscripts

Europe PMC Funders Author Manuscripts

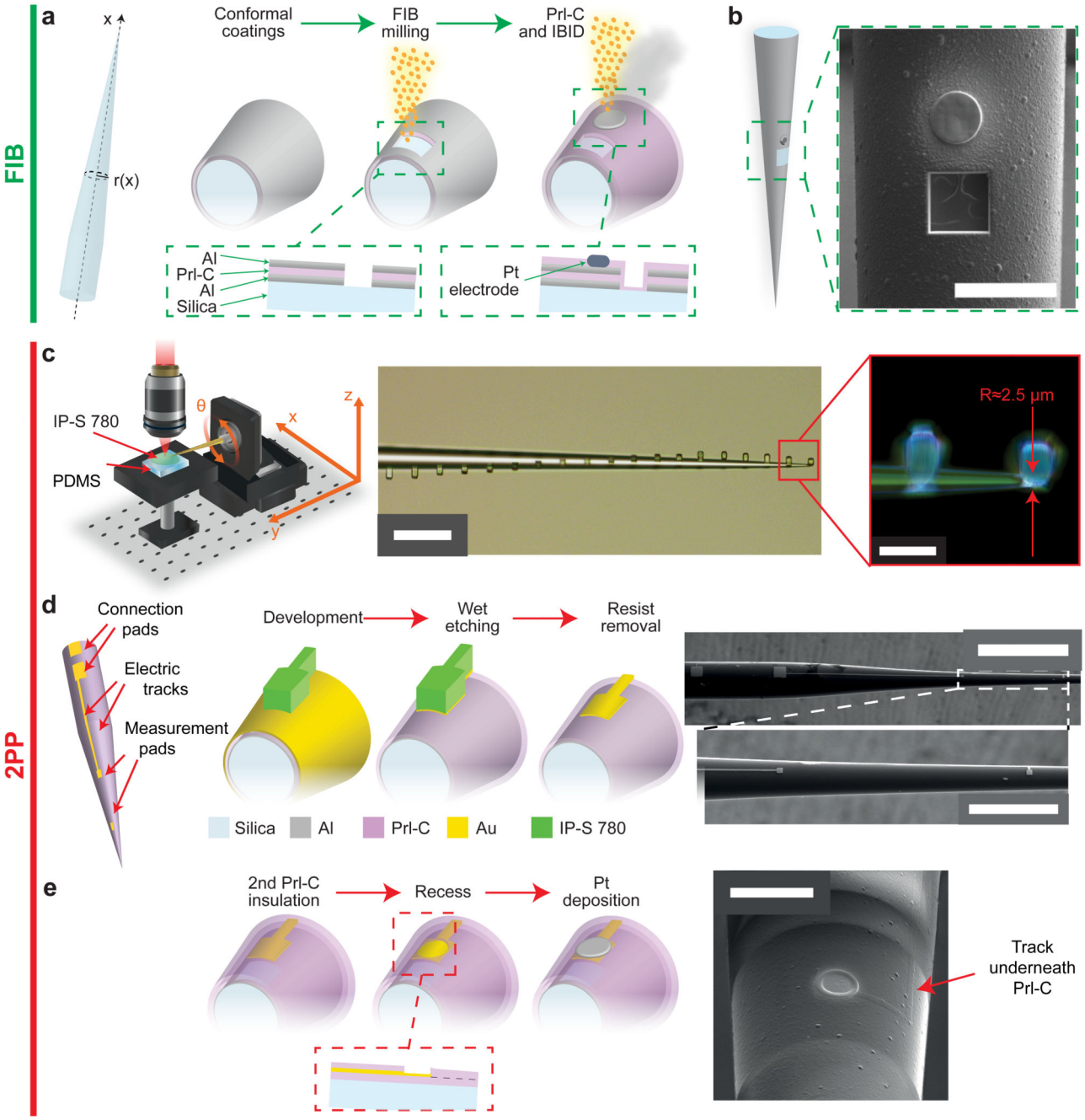


Figure 1. Fabrication process.

(a) Two Al layers are deposited on a tapered fiber, interleaved with an insulating Prl-C layer. FIB milling is employed to open the optical window. After depositing the final Prl-C coating, FIB milling and IBID are used to fabricate the electrode. **(b)** Final device configuration. Scale bar represents 30 μm. **(c) (left)** Sketch of the 4-axis piezoelectric stage allowing 360° patterning of the TF. **(right)** A series of 10 × 10 μm^2 base pillars realized around the taper. Scale bar is 100 μm. The inset shows the pillar realized at the smallest curvature radius, close to the fiber tip. Scale bar is 20 μm. **(d) (left)** Schematic of the

metallic patterns realized on the TF surface. **(center)** Sketch of the process steps in which a polymeric mask is fabricated through 2PP, followed by wet etching to remove the metal outside the mask and a resist removal step. The patterning was repeated independently n=3 times with similar results. **(right)** SEM micrographs of two separate metallic patterns (scale bar 500 μm). The measurement pads are separated by 700 μm, as shown in the inset. Scale bar for the inset is 200 μm. **(e) (left)** Schematic of the insulation step by Prl-C conformal coating, followed by the fabrication of a recess in correspondence of the measurement pad and Pt deposition, to tune the electrode impedance. **(right)** SEM micrograph of a representative electrode. The arrow highlights the electric track underneath the insulation Prl-C layer. Scale bar is 40 μm.

Europe PMC Funders Author Manuscripts

Europe PMC Funders Author Manuscripts

Europe PMC Funders Author Manuscripts

Europe PMC Funders Author Manuscripts

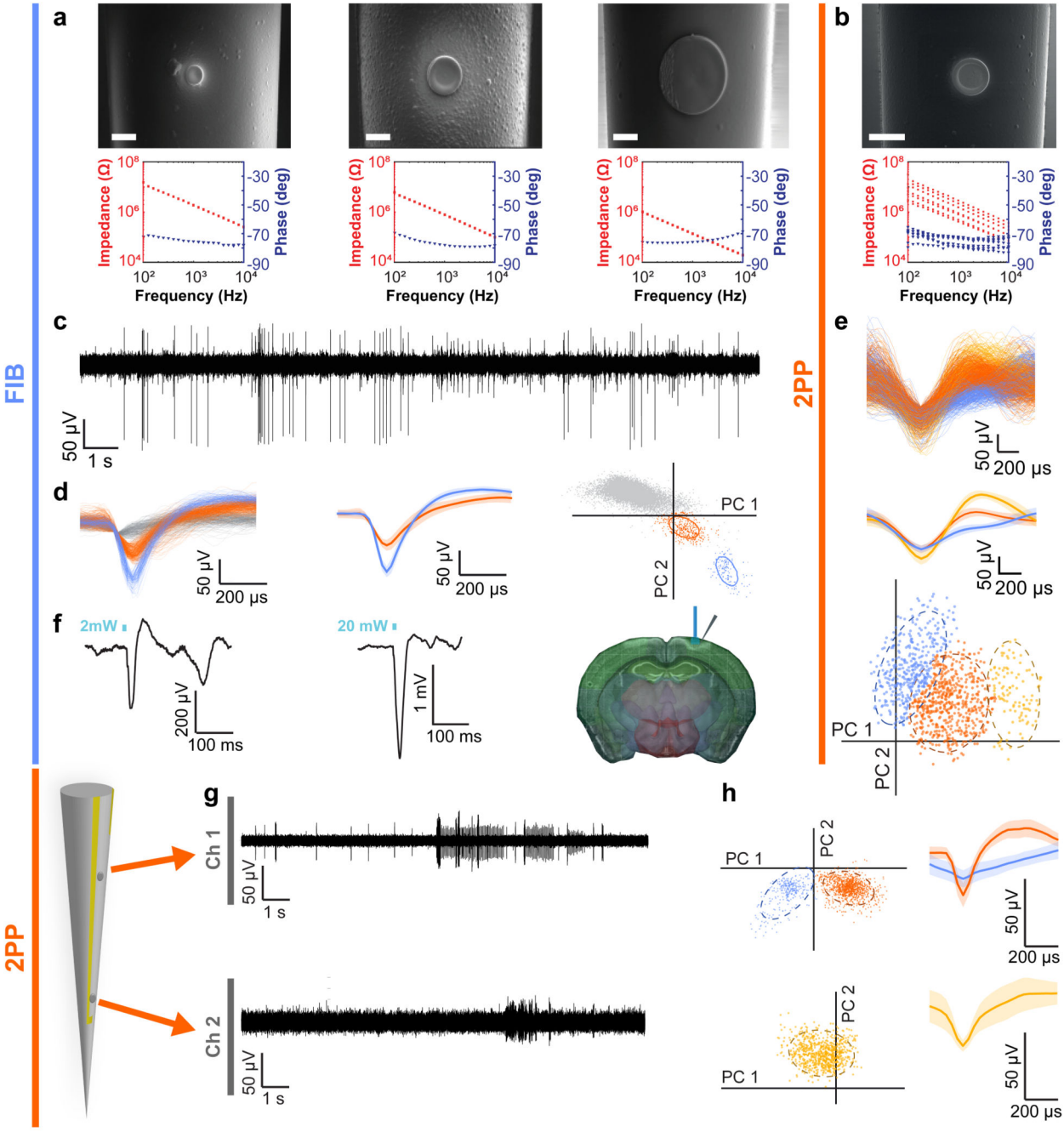


Figure 2. Electrical characterization and Extracellular recordings.

(a) SEM micrographs of Pt electrodes (diameters 7.5 µm, 15 µm and 30 µm) realized with the FIB milling process. Scale bars 10 µm. Impedance characterization in the graphs below. **(b)** SEM micrograph of a Pt electrode, diameter of 15 µm, realized with 2PP and impedance characterization (n=7 probes). **(c)** Representative high-frequency recording (300 Hz–10 kHz), 15 µm electrode, head-fixed awake mouse. **(d)** Single-unit spike sorting, left to right: sorted spikes, WT mouse n=1, unit a (green)=138 spikes, unit b (red)= 410 spikes; their mean (bold line) and standard deviation (STD, shaded area); PCA per-unit sort quality: L-

Europe PMC Funders Author Manuscripts

Europe PMC Funders Author Manuscripts

$Ratio_a$=0.0004, L-$Ratio_b$=0.00007; isolation distance isoD = 27.99. Cluster cutting ellipses displayed 68% confidence. **(e)** Waveforms, their mean (bold line) and STD (shaded area), and PCA clustering for three different neurons recorded during spontaneous activity in the range 250 Hz–10 kHz, anesthetized control mouse (signal-to-noise ratio SNR=11.17, noise standard deviation σ_{noise}=21.8 μV). Spike sorting returned 1075 waveforms. Sorted spikes: unit a (red)=577, unit b (green)=392, unit c (blue)=106. Per-unit sort quality: L-$Ratio_a$=0.04, L-$Ratio_b$=0.06, L-$Ratio_c$ =0.05; isolation distance isoD=12.3. Cluster cutting ellipses 95% confidence. **(f)** Representative LFPs (1-100Hz) recorded with the same electrode of Panels C and D, in Thy1-ChR2 cortex. Traces represent average of n = 5 and n = 3 stimulation with 2 mW and 20 mW light power (1 representative recording in 1 mouse, pulse duration 10 ms). Averaging was performed in IgorPro using raw data (no post filtering or baseline subtraction). Experimental configuration is shown on the right side of the panel: light delivered on top of the dura mater while recording neural activity in L2/3. **(g)** Highpass filtered traces (butterworth, 4^{th} order, cutoff 300 Hz, SNR_{CH1}=13.6, $\sigma_{noise,\ CH1}$=3.54 μV, SNR_{CH2}=8.77, $\sigma_{noise,\ CH2}$=6.56 μV) of spontaneous activity recorded in anesthetized control mouse (electrodes diameter 15 μm). **(h)** Related PCA and waveforms mean (bold line) and STD (shaded area) of two putative units recorded in L5 and L2/3 respectively. Sorted spikes Ch1:, unit a (green)=336 waveforms, unit b (red)=1172. L-$Ratio_a$=0.0004, L-Ratio =0.00007, isoD=39.4. Ch2: unit a=795 waveforms. Cluster cutting ellipses 95% confidence.

Europe PMC Funders Author Manuscripts

Europe PMC Funders Author Manuscripts

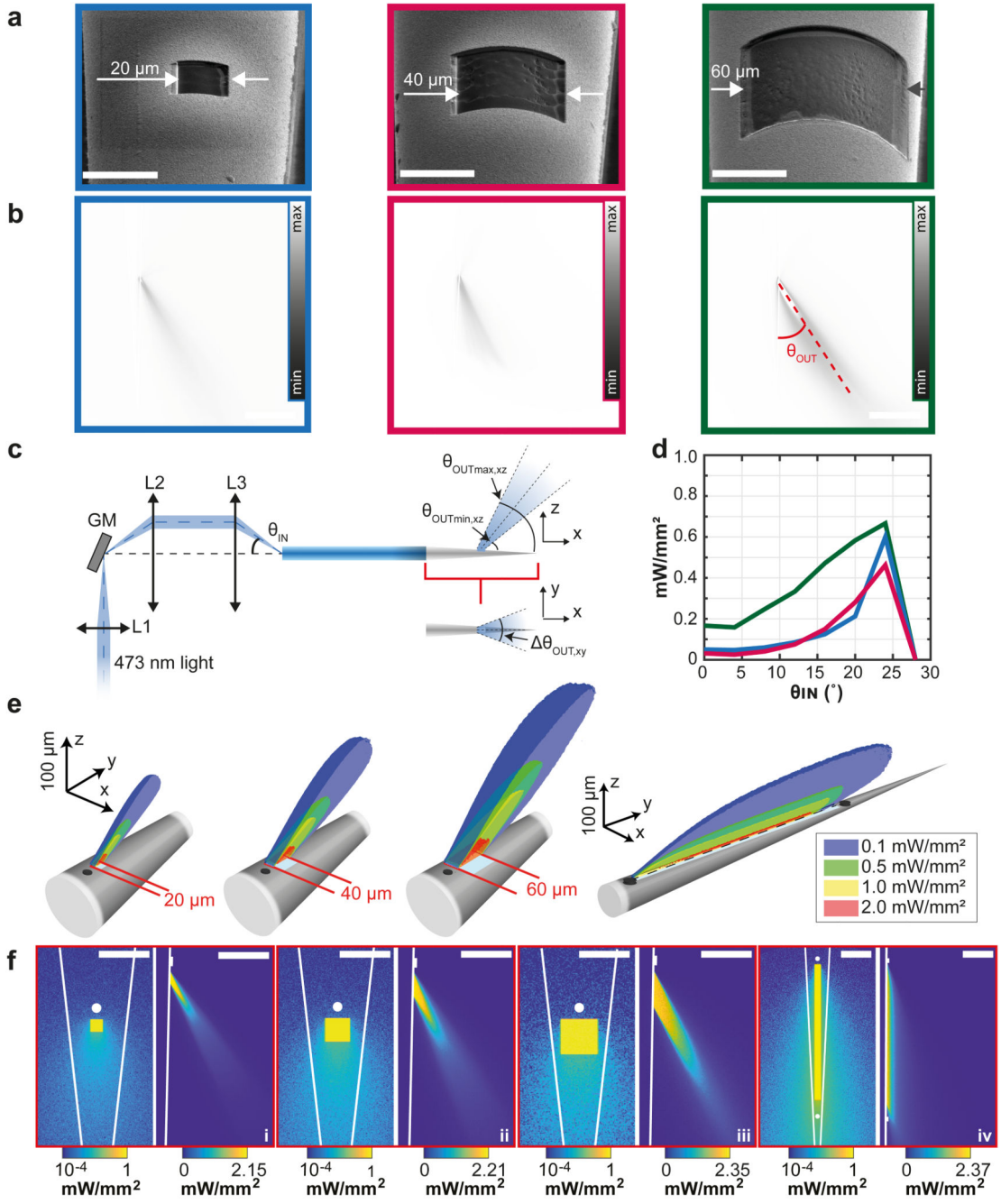


Figure 3. Light emission properties in quasi-transparent solutions and related Monte Carlo simulations in scattering brain tissue.

(a) SEM micrographs of the realized optical windows (from left to right sizes are 20×20 μm^2, 40×40 μm^2 and 60×60 μm^2). Scale bar represents 30 µm. (b) Emission patterns characterized in a 30 µM fluorescein:PBS bath for each window size, at input angle maximizing emission intensity. Experimental output angle θ_{OUT} is ~24° for the investigated window sizes (fiber numerical aperture 0.39). (c) Schematic of the light injection setup used for in vitro experiments. GM is a galvanometric mirror used to deflect the beam. Lens L1 focuses the beam on the GM, lens L2 collimates the beam while lens L3 focuses light onto

the fiber core with a specific input angle. (d) Power density values measured at the window exit for different θ_{IN}. Similar results were obtained independently on n=3 devices for all panels. (e) Iso-intensity surface maps at 0.1 mW//mm^2, 0.5 mW/mm^2, 1.0 mW/mm^2 and 2.0 mW/mm^2 of the simulated light emission distribution for three different windows sizes (20 × 20 μm^2, 40 × 40 μm^2, and 60 × 60 μm^2 μm from left to right) and a rectangular slot (500 × 20 μm^2, input angle 24°, see Supplementary Figure 4 for optical characterization) simulated by a Monte Carlo approach. Data are shown for an average power density emitted from the apertures of 2 mW/mm^2. (f) Power density distributions for three different windows sizes (20×20 μm^2, 40×40 μm^2, and 60×60 μm^2 in subpanels i, ii, iii, respectively) and slot aperture, iv) at the fiber surface (left, logarithmic colormap) and in a meridional plane cutting the aperture in two halves (right, linear colormap). Data are shown for an average power density emitted from the apertures of 2 mW/mm^2. Scale bar is 100μm. Simulations were run with values $\theta_{OUTmin,xz}$ = 25°, 21°, 27°, and 8°, $\theta_{OUTmax,xz}$ = 42°, 38°, 33°, and 24°, $\Delta\theta_{OUT,xy}$ = 18°, 24°, 30°, and 18°, for 20 × 20 μm^2, 40 × 40 μm^2, 60 × 60 μm^2, and 500 × 20 μm^2 apertures, respectively.

Europe PMC Funders Author Manuscripts

Europe PMC Funders Author Manuscripts

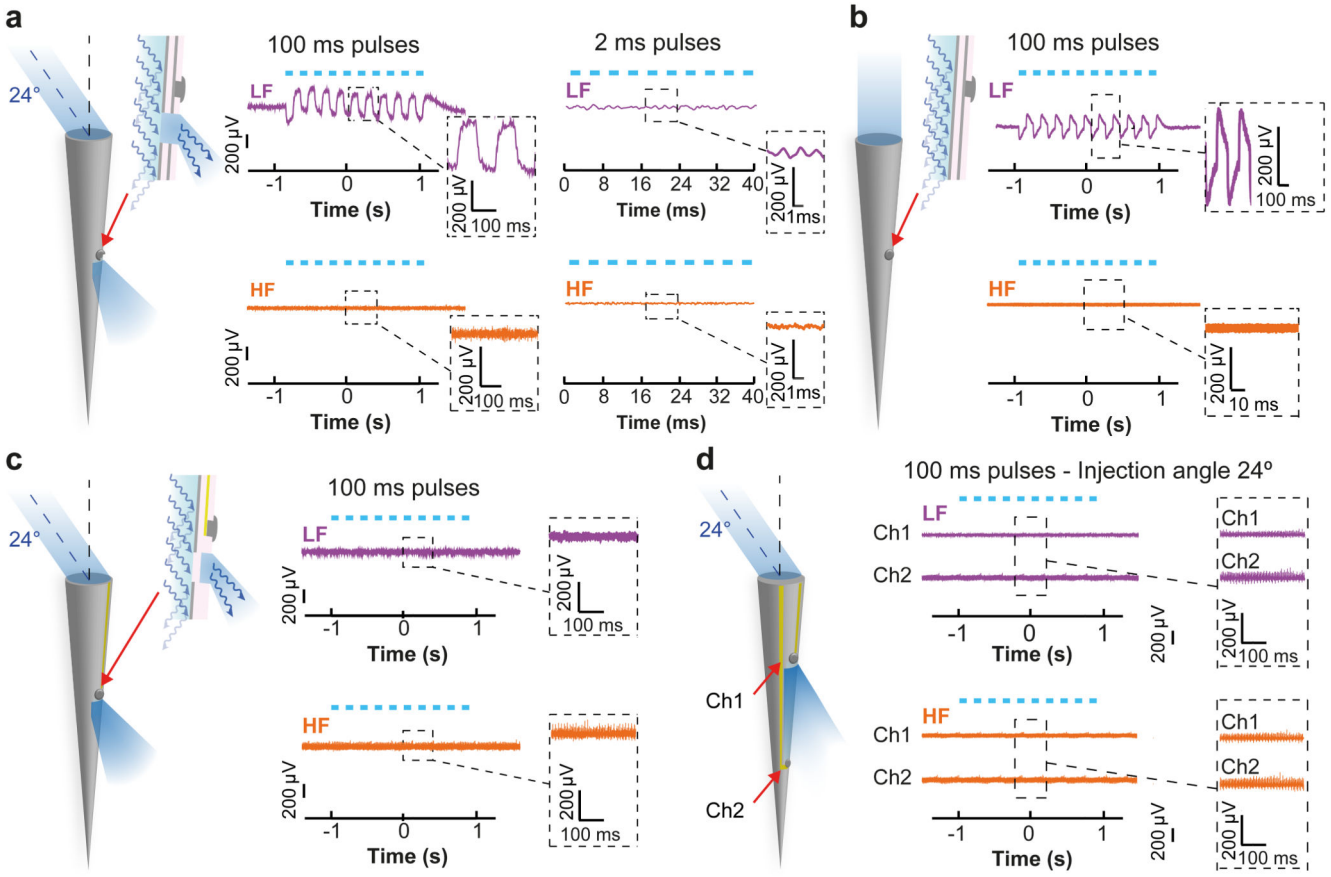


Figure 4. Light-induced photoelectric noise in PBS for low frequency (LF) and high-frequency (HF) channels

for: **(a)** a fibertrode tested with both 100 ms and 2 ms light pulses, with light injection at θ_{IN} = 24°; **(b)** a fibertrode with no optical window tested with 100 ms light pulses and full-NA light injection; **(c)** a fibertrode fabricated with 2PP, featuring one window and one electrode, θ_{IN} = 24°; **(d)** a fibertrode fabricated with 2PP, featuring two electrodes and a rectangular slot-like aperture, θ_{IN} = 24°.

Europe PMC Funders Author Manuscripts
Europe PMC Funders Author Manuscripts

Europe PMC Funders Author Manuscripts

Europe PMC Funders Author Manuscripts

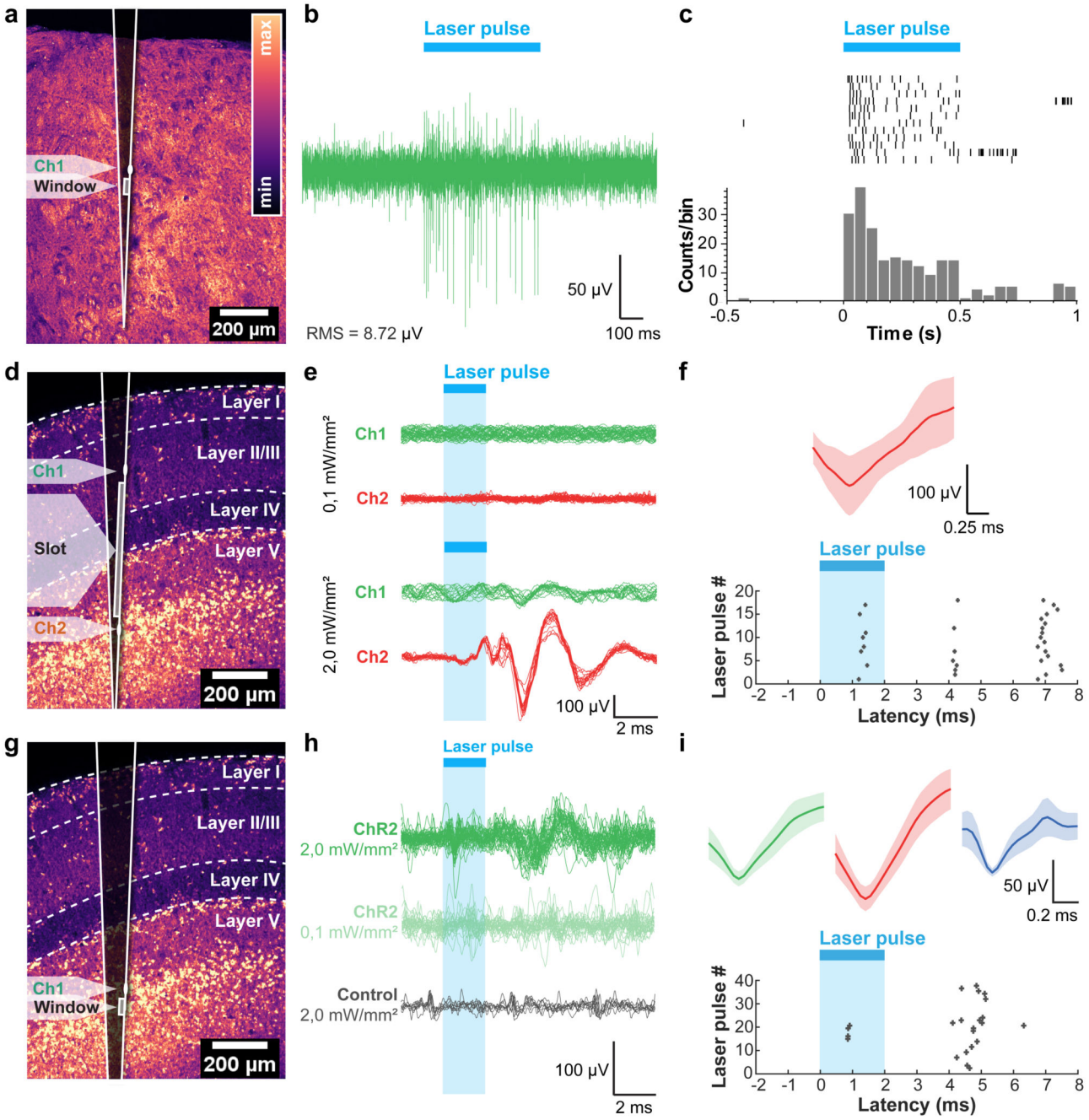


Figure 5. ***In vivo*** **test of the fibertrode.**

(a) Superposition of two-photon image of a 300 µm-thick slice and a fibertrode sketch, showing implant depth. **(b)** Representative trace and raster plot of action potentials recorded in striatum n = 3, with a fibertrode containing 7 µm electrode pad and 40 × 40 μm^2 optical window in response to continuous 500 ms optical pulse. For data in panels B and C inter-trial interval is 30 s. **(c)** Average peristimulus histogram of the number of action potentials. **(d)** Superposition of two-photon image of a 300-µm thick slice of Thy1-ChR2-YFP mice and a fibertrode sketch, showing implant depth and slot extent through the cortex. **(e)**

Europe PMC Funders Author Manuscripts

Europe PMC Funders Author Manuscripts

Overlapped 12 ms long traces aligned at the onset of the laser (2 ms long pulse) at 0.1 mW/mm^2 (upper traces) and 2 mW/mm^2 (lower traces) for both the electrode placed in L2/3 (green) and the electrode placed in L5 (red). (SNR_{CH1} = 6.79 $\sigma_{noise,\ CH1}$ = 8.8 μV, SNR_{CH2} = 11.85, $\sigma_{noise,\ CH2}$ = 19,7 μV). **(f)** Waveform of the sorted unit (mean in bold line, shaded area represents standard deviation). Sorted spikes = 163. Latency of triggered spikes for each laser pulse is reported below. **(g)** Superposition of two-photon image of a 300 μm-thick slice of Thy1-ChR2-YFP mice and a fibertrode sketch, showing implant location. For data in panels **e** and **f** inter-trial interval is 1 s. **(h)** Overlapped 12 ms long traces aligned at the onset of the laser (2 ms long pulse) at 0.1 mW/mm^2 (upper traces) and 2 mW/mm^2. Control was run in a ChR2-negative mouse, threshold was set at 4σ for all sortings. (Green traces: SNR = 8.37, $\sigma_{noise,\ CH1}$ = 13.22 μV; gray trace $\sigma_{noise,CH1}$ = 5 μV). **(i)** Waveform of the sorted unit for a 180 s long recording (mean in bold line, shaded area represents standard deviation). Sorted spikes: unit a (green) = 1435, unit b (red) = 436, unit c (blue) = 1247. Latency of triggered spikes for each laser pulse is reported below. For data in panels H and I inter-trial interval is 1 s. PCA and sorting quality metrics are shown in Supplementary Figure 6.

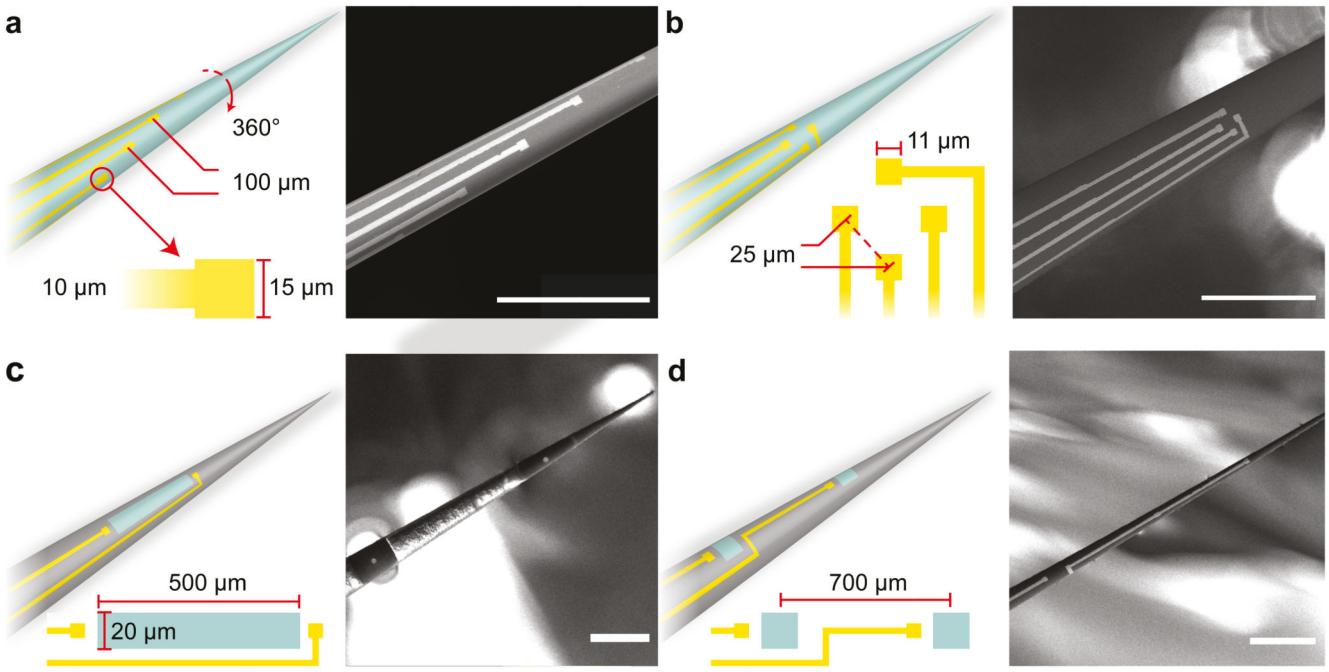


Figure 6. Scalability of the 2PP based patterning process.

Sketch and SEM images of different fibertrode designs. **(a)** Fibertrode featuring parallel metal tracks of different lengths resulting in spiral electrode distribution all around the taper; **(b)** fibertrode with tetrode configuration; **(c)** fibertrode featuring a 500 µm long window with two electrodes placed at the slot ends; **(d)** fibertrode with two light emission sites, each one paired to one electrode fabricated just above the optical window. For each panel, scale bars indicate 200 µm. Patternings in all panels were repeated independently n=3 times with similar results.

Europe PMC Funders Author Manuscripts
Europe PMC Funders Author Manuscripts